Ultrasonic Spray Coating for the manufacturing of a selective layer for flow batteries: From the analysis of ink composition to component scale-up

Marco Cecchetti [a],[*], Simone Fiorini Granieri [a],[b], Fabio Di Fonzo [a],[b], Damiano Fustinoni [a], Alfonso Niro [a], Andrea Casalegno [a], Matteo Zago [a]

[a] Politecnico di Milano, Department of Energy, Via Lambruschini 4, 20156 Milano, Italy
[b] Center for Nano Science and Technology, Istituto Italiano di Tecnologia, Via Rubattino 81, 20134, Milano, Italy

HIGHLIGHTS

- A selective layer for thin membrane for Vanadium Redox Flow Battery was developed.
- Ultrasonic Spray Coating was investigated as manufacturing process.
- The ink composition and the manufacturing process were investigated.
- The scalability of the process and of the selective layer were investigated.
- The selective layer can effectively reduce vanadium cross-over at all scales.

ARTICLE INFO

ABSTRACT

Developing highly selective separators that can effectively mitigate vanadium crossover is crucial for improving Vanadium Redox Flow Batteries (VRFB), which can play a key role in tackling the challenges set by future energy scenarios. This work presents the development of the barrier, a selective layer directly deposited on the membrane, using Ultrasonic Spray Coating (USC). Ultrasonic Spray Coating is characterized by excellent flexibility, allowing for easy deposition on any kind of substrate and enabling the tuning of the barrier ink composition. Moreover, as a commercial and already scaled-up technique, USC is suitable for the large-scale manufacturing of the barrier layer. Indeed, this work demonstrates the development of the barrier through USC starting from lab-scale to a size more representative of real applications. The composition of the ink and the deposition process were investigated to define the best ink composition and best combination of deposition parameters for the barrier scale-up. The barrier was directly deposited on *Nafion*[TM] NR212, successfully reducing the capacity decay of the battery and the net vanadium flux by around 30 % without penalizing efficiency. Finally, the barrier layer effectively mitigated cross-over losses also at larger scale, with improved battery efficiency when deposited on a thinner membrane (*Nafion*[TM] NR211).

1. Introduction

The evolution of the global energy scenario in the next years foresees an increase in the production of energy from renewable energy sources. Indeed, in 2023 the global annual addition of capacity from renewable sources increased up to 510 GW (~+50 % with respect to 2022) and it is forecasted to increase up to 710 GW in 2028 (~+110 % with respect to 2022) [1]. Wind and solar PV are leading this increase in installed capacity contributing more than 90 % of the annual additions [1]. The intermittent and non-programmable nature of these energy sources set challenges for the management and the security of the electric grid: therefore, reliable and efficient large-scale energy storage systems are required to face these challenges [2,3]. In this scenario, scalability and fast response time make electrochemical energy storage technologies an effective solution for a wide range of power and energy ratings [4]. Among these technologies Vanadium Redox Flow Batteries (VRFB) is a promising technology due to the advantages it presents with respect to other types of battery systems such as independent energy to power

ratio, long cycling life, low safety related issues, no fire hazard and complete recyclability of the electrolytes [4,5].

Despite these advantages, the commercialization of the technology is hindered by some drawbacks such as low energy and power densities, resulting in high capital costs [6,7]. The low values of energy density (20–30 Wh l^{-1}) and power density (1.5–2 kW m^{-2}) are caused by some technological issue and limitations: solubility of vanadium ions in the electrolyte [8,9], vanadium cross-over [10–13], shunt current losses [14,15], ohmic losses through the separator [14,16,17], reactants distribution over and inside the porous electrodes [9,18–20] and activity of the carbon-based electrodes [21,22].

In this work, the focus is on vanadium cross-over, which is the undesired permeation of vanadium ions through the not-ideally selective separator of a Vanadium Redox Flow Battery (VRFB) that leads to side reactions of self-discharge, causing electrolyte imbalance and capacity loss for the battery [9,11,13]. Despite being a reversible phenomenon in VRFB by rebalancing procedures [11,23], it is an issue that must be mitigated to maximize the stored and dispatched energy during the lifetime of the battery, to minimize efficiency loss due to unbalanced operation and operating and maintenance costs related to the rebalancing procedures [11]. The most common and straightforward strategy for mitigating cross-over losses is properly designing the ionic separator taking into account its proton conductivity, selectivity and cost [16]. High proton conductivity and excellent mechanical and chemical stability in acidic environment promoted the employment of *Nafion*^{TM} cation exchange membranes in VRFB applications. However, the low selectivity towards vanadium forces the employment of relatively thick membranes, penalizing the power density and increasing the systems costs [16,24–27]. Alternatives to *Nafion*^{TM} membranes are either low-cost cation exchange membranes based on sulfonated polymers or hydrocarbon-based anion exchange membranes, which both offer the advantage of lower vanadium permeability with respect to *Nafion*^{TM}. However, these types of membranes present lower ion conductivity, penalizing the voltage efficiency of the battery [17,27,28]. Countless works can be found in literature proposing innovative alternative solutions to solve the compromise between selectivity, battery efficiency and system costs. The most common strategies investigated in literature are the application of a dense layer on a porous separator [29–34] and the modification of the membrane, usually with nanofillers in the polymeric matrix [35–43].

The works presented in literature focus either on improving the conductivity or reducing the vanadium permeability, usually without discussing an important technological aspect: the scalability of the separator and of its fabrication process. Indeed, in literature this aspect is not usually discussed, and the proposed solutions are often demonstrated only at lab-scale, a few examples: 4 cm^2 and 5 cm^2 [30,31,34, 44], 9 cm^2 [40,45–47], 13.5 cm^2 [36,37,39,41], 25 cm^2 and 48–49 cm^2 [32,33,42,48,49].

In previous works [50,51], the authors presented a different solution consisting in the direct deposition of a thin selective layer (~2 μm) over commercial *Nafion*^{TM} membranes. The selective layer, describe in the patent application WO 2019/197917 and referred as "barrier", is composed of *Nafion*^{TM} ionomer, acting as a binder and promoting proton conductivity, and a mixture of nanoparticles of different dimensions, such as Vulcan® XC-72R and silica nanoparticles. Because of the mixture of nanoparticles, the barrier introduces a tortuous path for the ion transport through the separator, mitigating the permeation of vanadium ions by increasing their mass transport resistance and improving thus the selectivity of the membrane. Indeed, since the protons have a smaller hydration shell than vanadium ions [52], the introduction of a tortuous path affects them less than vanadium ions. The combination of nanoparticles of different sizes favours the selectivity of the barrier, as the smaller nanoparticles can fill the gaps between the larger nanoparticles, enhancing the tortuosity of the layer. In the previous works, the authors manufactured the barrier layer through Reactive Spray Deposition Technology (RSDT), a flame-based spray coating technique, and they demonstrated the ability of the barrier layer to effectively mitigate cross-over losses, reducing the cross-over losses and the self-discharge of the battery, allowing to reduce the thickness of the membrane, reducing costs without sacrificing the efficiency of the battery [50,51].

In this work a further step in the development of the barrier layer is presented. In particular, the design, manufacturing and development of the barrier layer via Ultrasonic Spray Coating (USC) is investigated. The goal is to demonstrate not only that the barrier layer can be manufactured with an alternative deposition technique, but that it can be also scaled-up from lab scale to a scale more representative of the real operation. USC is a spray coating technique that exploits a vibrating tip of the nozzle for a high degree of atomization of the liquid droplets of an ink to obtain a uniform coating. USC is exploited for ultrasonic coating of thin films in industrial applications such as alternative energy and nanomaterials applications (fuel cells, electrolysers, solar cells and sensors), glass and industrial applications (functional and protective coatings, lenses and automotive), medical applications and semiconductors [53–58]. USC has the advantage of being a commercial and an already scaled-up technique, since it can be employed for both research purposes and high-volume productions. Moreover, this technique guarantees an excellent flexibility as it allows to directly deposit on any kind of substrate, to easily tune the properties of the ink and the parameters of the deposition process to obtain the desired coating.

This works is structured as follows: in the first phase the ink was analysed to define the best composition in terms of quality of the coating, battery self-discharge mitigation and battery efficiency, then the deposition process was investigated aiming for the scale-up of the barrier layer to a scale more representative of the real applications. Indeed, in the first phases the barrier layers were manufactures with an active area of 4 cm^2 to facilitate the screening of different ink compositions. Subsequently, the size of the barrier layer is increased up to 100 cm^2 and tested in a VRFB to evaluate the scalability of the process and the ability of the barrier to mitigate cross-over phenomena also at a scale more representative of the real applications. Finally, the barrier layer was deposited on a thin membrane, *Nafion*^{TM} NR211 (25 μm thick), in order to assess the ability of the barrier to improve the selectivity of thinner membranes, in order to enable their use in commercial applications to reduce costs and improve the efficiency of the battery.

2. Experimental

2.1. Barrier manufacturing via ultrasonic spray coating

The barrier samples were manufactured by directly depositing the corresponding ink on *Nafion*^{TM} NR212 membranes with an *ExactaCoat OPIII* machine by *Sono-Tek*$^{(C)}$ equipped with an *AccuMist*^{TM} ultrasonic nozzle, an ultrasonicated syringe *SonicSyringe*^{TM} and a vacuum heated plate. The inks were prepared by mixing in a glass bottle an equal amount of Vulcan® XC-72R nanoparticles (*Fuel Cell Store*, ~40 nm) and silica nanoparticles (*Merck Life Science*, ~20 nm), accordingly to Cecchetti et al. [51], with a *Nafion*^{TM} D2021 dispersion (20 wt%, *IonPower*). Vulcan® XC-72R and silica nanoparticles provide the tortuous path for the mitigation of vanadium ions transport, while the *Nafion*^{TM} ionomer supports the proton conductivity and acts as a binder between the different nanoparticles and it bonds the barrier layer itself to the membrane [50,51]. Moreover, using the same ionomer as the membrane for the barrier layer minimize the risk of delamination of the coating by removing the differences in the swelling ratios of the support and of the coated layer in aqueous environments [51]. The amount of added dispersion varied with each barrier layer accordingly to the desired Ionomer-to-Nanoparticles mass ratio (IN Ratio) as reported in Table 1. Finally, ethanol (Absolute anhydrous RPE-ACS, *Carlo Erba Reagents*) was added to the ink as dispersing solvent accordingly to the desired Solvent-to-Nanoparticles ratio (SN ratio). The inks were then bath sonicated for 2 h in water at ~0 °C in an ultrasonic bath at maximum power (*Bronson 2800 CPXH*) and immediately loaded to the ultrasonicated

Table 1
Ink composition (Ionomer-to-Nanoparticles and Solvent-to-Nanoparticles ratios) of the tested barrier samples for the analysis of the ink composition.

Barrier Sample	IN [−]	SN [ml/g]
A	1	175
B	2	175
C	4	175
D	4	60
E	4	485

syringe and fed to the ultrasonic nozzle.

All barrier samples were directly deposited on only one side of a *Nafion*^{TM} membrane with the desired active area. The supporting *Nafion*^{TM} membranes were placed directly on the heat-plate and were kept in place by the vacuum generated by the heat-plate, while a glass-PTFE mask delimited the active area. Indeed, the total deposited area was wider that the active area of the barrier and part of the ink was deposited on the glass-PTFE mask to ensure a complete and homogeneous filling of the intended area. The deposition pattern consisted of unaligned identical horizontal serpentines with a vertical offset for filling the voids of each serpentine path to achieve a uniform coating. Between each serpentine, the nozzle was moved away from the heat-plate for 5 s to allow the drying of the deposited ink. Once the deposition was completed the barrier samples were let rest on the heat-plate for 30 min to ensure a complete evaporation of the solvent.

It is worth mentioning that an initial phase of the work was conducted to acquire confidence with the USC technique, to design the deposition patterns according to the ink composition and deposition process parameters, as well as a proper sensitivity on the different parameters involved in terms of both ink composition and deposition process and on their interactions. Indeed, different the ink formulation largely influences the deposition process: the swelling of the membrane, the time required for solvent evaporation and atomization power are dependent on the ink composition and dispersing media. This process, which is not reported in this work for sake of simplicity, allowed to define the starting point and the range of the parameters for the ink composition and the deposition process, which were tuned in the framework of the activities reported in this work.

2.1.1. Barrier manufacturing for ink composition analysis

Different inks were prepared to investigate the influence of the ink composition on the morphology of the barrier and its performance in the battery in terms of battery efficiency and cross-over mitigation. In this phase of the work the focus was on the effect of the amount of ionomer in the barrier layer and the dilution of the ink. Table 1 reports the barrier layers manufactured in this phase and the composition of the corresponding ink.

The study of the effect of the ink composition on the properties of the barrier was performed on samples of active area 4 cm^2 (2x2). The deposition pattern for each sample consisted in two serpentines with 2 mm distance between the lines of each serpentine and 1 mm offset between the two serpentines. This double-serpentine pattern was repeated different times to achieve the desired thickness of 10 ± 1 µm according to the concentration of the ink to obtain the same amount of dry fraction deposited on the membrane. In particular, the number of pattern repetitions were ten times for samples A, B and C while samples D and E were deposited with two and fourteen repetitions respectively. The ink was deposited from a height of 27.5 mm with a rate of 0.2 ml min^{-1} and a nozzle translational speed of 20 mm s^{-1}, while the atomization power of the nozzle was set to 2.3 W and the shaping gas flow rate to 5 l min^{-1}. The heat-plate temperature was set to 60 °C for each sample. After the deposition, the samples were left of the heat-plate for 30 min to allow the complete evaporation of the solvent. For each barrier samples a 1 cm^2 barrier sample was deposited on a piece of silicon wafer for morphological characterization through SEM.

Both deposition pattern and deposition parameters were defined after a preliminary analysis on the effect of those parameters on the quality of the coating and to prevent the swelling of the membrane due to the solvent.

2.1.2. Barrier manufacturing for the analysis of ink flow rate

After identifying the ink composition ensuring the best barrier performance, it was used to manufacture two barrier samples with different ink flow rates and nozzle velocity to investigate the effect of increasing the ink flow rate on the barrier properties and performance. The goal is to verify if it is possible to manufacture an effective barrier layer with a higher ink flow rate to reduce the time required for the deposition process, which is a critical parameter for the scale-up of the process at industrial level.

Since the scale of the manufactured samples influences the deposition process, in this phase of the work the active area of the barrier layer was increased to 25 cm^2 (5x5) to be closer to the real applications without abandoning the lab-scale for the investigation of the parameters.

The first barrier sample realized in this phase of the work was manufactured with ink flow rate of 0.2 ml min^{-1}, nozzle speed of 20 mm s^{-1}, nozzle height 27.5 mm and heat-plate temperature of 60 °C, i.e. the same deposition process parameters as the ones in Section 2.1.1. The deposition pattern was not changed with respect Section 2.1.1, but simply enlarged to adapt it to the new size of the samples. The second barrier sample was manufactured by increasing the ink flow rate to 0.5 ml min^{-1}, while the nozzle translational speed was increased proportionally to 50 mm s^{-1}. It was not possible to increase only the flow rate, because keeping the velocity at 20 mm s^{-1} led to the flooding of the substrate and consequent intense swelling of the supporting membrane. Moreover, it was necessary to reduce the height of the nozzle from 27.5 mm to 5 mm due to the instability in the spray cone to the high translation speed of the nozzle. Moving the nozzle closer to the substrate reduces the cone area of the spray, thinning thus the ink trail from 4 mm to 2 mm. This required a change in the deposition pattern as the one used previously did not guarantee a uniform coating as the spacing between the serpentine lines was too large, resulting in a striped coating. Moreover, reducing the distance between the nozzle and the substrate made issues related to the shaping gas impingement on the substrate rise. Indeed, the shaping gas reached the substrate with higher velocity and pressure displacing the wet ink deposited in the previous serpentine line. Therefore, the deposition pattern was modified in ten horizontal serpentines with 5 mm spacing between the lines of each serpentine with a vertical offset of 0.5 mm between each serpentine. This pattern was repeated three times to obtain a thickness closer to the barriers manufactured with the first deposition pattern. A visual representation of the deposition patterns is reported in the Supplementary Materials (Fig. S1).

2.1.3. Barrier manufacturing for the scale-up at 100 cm^2

After identifying the best ink composition and the best combination of ink flow rate and nozzle velocity, a barrier of 100 cm^2 (6.8x14.7) active area was deposited on *Nafion*^{TM} NR212 to investigate the scalability of the process and to validate the cross-over mitigating ability of the barrier also at a scale more representative of the real applications, which can reach cell active areas between 600 cm^2 and 1200 cm^2. Moreover, a similar barrier layer was deposited on a thinner membrane, *Nafion*^{TM} NR211 (25 µm thickness) to assess the ability of the USC the deposit an effective barrier also on thin substrates.

The deposition process was kept the same as before, with the only change of removing the waiting step between each serpentine, as the time required to make a serpentine was enough to cover it and to let the ink dry.

2.2. Morphological characterization

Plain view and cross-section view of the barrier samples on silicon

wafers were obtained by Scanning Electron Microscopy (SEM) with either a MIRA 3 TESCAN and a ZEISS SIGMA 500 electronic microscopes. The latter was also used for Energy Dispersive X-ray Spectroscopy (EDS). SEM images were acquired at different magnifications with 5 kV voltage and walking distance of 2.70 mm.

Silicon wafers as support allowed to obtain more clear images of the barrier layers than *Nafion*[TM] due to the better electric conductivity. Moreover, silicon wafers allowed to obtain clear cross-section view of the barrier layers without the need of cryogenic fracturing.

The following subsections describe the experimental set-up and testing for the characterization of the performance of the barrier layers in VRFB for the different phases of this work.

2.3. Electrochemical characterization for ink composition investigation

2.3.1. Experimental set-up

During the investigation of the ink composition, the barrier samples were tested in a VRFB with active area of 4 cm^2 with serpentine flow fields at both positive and negative side of the cell. Carbon paper electrodes (*Sigracet® 39AA*, nominal thickness 290 µm) were used as both positive and negative electrodes compressed to 230 µm with glass-PTFE gaskets (*PTFE-impregnated fiberglass, Maspe S.A.S.*) [59]. A VRFB battery employing bare *Nafion*[TM] NR212 was tested as reference for the barrier samples. The *Nafion*[TM] NR212 membrane was used as received without any treatment. In all tests employing the barrier layer, the barrier layer was oriented towards the negative electrode.

The electrolyte solutions were prepared by dissolving vanadium (IV) sulfate oxide hydrate (*Alfa Aesar*) in 5 M sulphuric acid (*VWR*) to obtain 1 M of vanadium ions and by following the procedure illustrated by Aaron et al. [60]. The electrolyte solutions were processed with a Watson-Marlow 323Du peristaltic pump equipped with a 314Dw roller head pump. Moreover, the electrolyte solutions were pressurized with nitrogen to avoid air intake.

An UV–Vis–NIR PerkinElmer Lambda 950 UV–VIS–NIR spectrophotometer was used to measure the absorbance of electrolyte solutions to estimate the concentration of vanadium ions after a diffusion test by exploiting the Beer-Lambert Law [31,61–65]. The Lambda 950, a dual beam spectrophotometer, was able to perform measurements by comparing two quartz cuvettes of 10 mm optical depth: one with the tested electrolyte solution, the other with a reference solution of only sulphuric acid 5 M.

A high-precision high-speed source-measure unite (SMU) module *PXI-4139* equipped on a *NI PXIe-1082* chassis by *National Instruments* was used to perform charge-discharge cycles and Electrochemical Impedance Spectroscopy (EIS).

2.3.2. Experimental tests

Each barrier sample and the reference membrane were initially tested through diffusion test (Fig. 1A). The diffusion test consisted in circulating for 24 h an electrolyte composed of 1 M VO^{2+} ions in 4 M sulphuric acid at the positive side (rich side) of the battery with a flow rate of 9 ml min^{-1}, while at the negative side (poor side) only sulphuric acid (5 M) without vanadium. The presence of a concentration gradient between the two sides of the battery drives a flux of VO^{2+} ions through the separator, leading to non-null concentrations of vanadium ions in the poor side. In this way it is possible to estimate a mean vanadium flux through the membrane exploiting the molar balance at the poor side of the battery between the beginning and the end of the test:

$$\overline{N_{VO^{2+}}} = \frac{C_{VO^{2+}}^{poor\ side} V_{poor\ side}}{A_{cell} \Delta t} \tag{2.1}$$

with $C_{VO^{2+}}^{poor\ side}$ vanadium concentration at the poor side at the end of the diffusion test, $V_{poor\ side}$ volume of the sulphuric acid at the poor side (50 ml), A_{cell} active area of the battery and Δt duration of the test. The concentration of vanadium ions at the poor side at the end of the test was
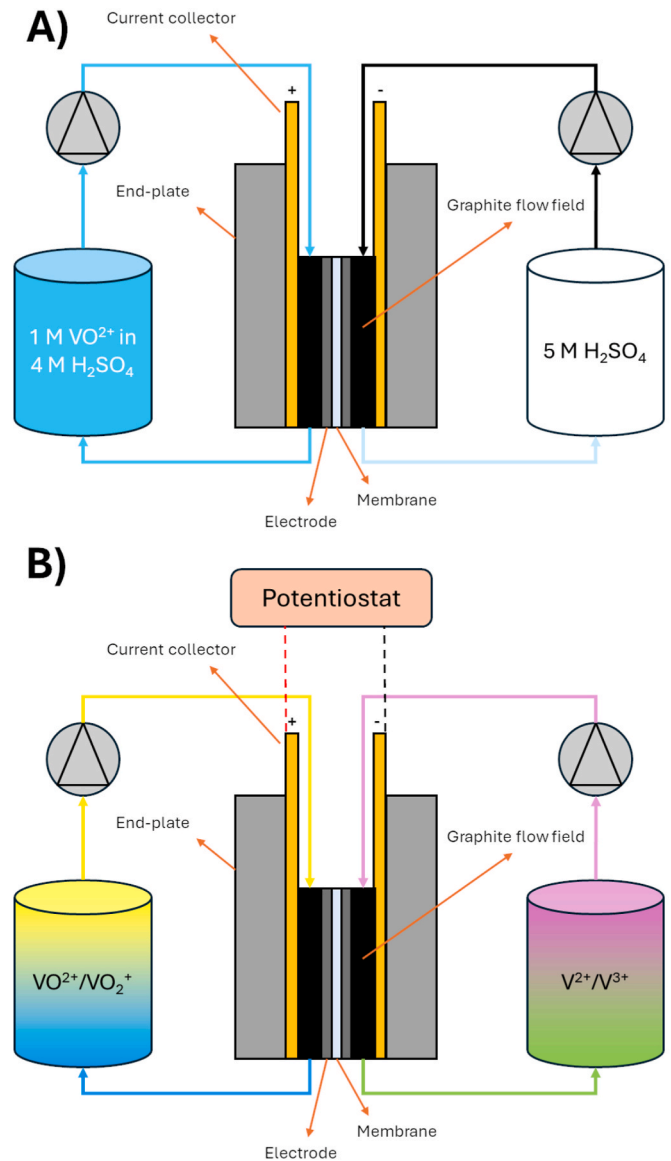

Fig. 1. – Experimental set-up for A) diffusion tests and B) electrochemical characterizations.

measured through UV–Vis spectrophotometry by measuring the absorbance of the poor side solution at the end of the test. Indeed, according to the Beer-Lambert Law:

$$A_\lambda = \epsilon_\lambda l C_{VO^{2+}} \tag{2.2}$$

where A_λ is the monochromatic absorbance, ϵ_λ the molar attenuation coefficient and l is the optical path length, which is the width of the glass cuvette in which the solution sample is hold. Since the different vanadium species have their own characteristic peak in the absorbance spectrum, this technique allows to easily measure the concentration of each vanadium species in a solution [61]. In particular, the peak of VO^{2+} is at wavelength in the around of 760 nm. The value of ϵ_λ for VO^{2+} is reported in literature to be around 0.018 $m^3 mol^{-1} cm^{-1}$ [61–63]. However, to obtain a more accurate measure a calibration of the absorbance-concentration relationship was performed to obtain the value of the molar attenuation coefficient ϵ_λ at 758 nm.[1] The calibrated

---

[1] The peak of the absorbance spectra occurred at 758 nm in the operating conditions of this work.

value of the attenuation coefficient was calculated to be 0.01827 $m^2\ mol^{-1}\ cm^{-1}$, coherent with the literature values. The calibration process was reported in the Supplementary Materials.

Following the diffusion test, each separator was tested in charge-discharge cycles with fixed charged and discharged capacity at constant current of 50 mA cm^{-2} (Fig. 1B). The exchanged capacity was set to 750 C, around 40 % of the ideal capacity of the electrolyte solutions, whose volume was 20 ml. The starting SoC of the electrolyte solution was 40 %, while the volumetric flow rate was set to 9 ml min^{-1}. As described in previous works of the authors [50,51,66,67], this type of cycles allow to separate the self-discharge of the battery due to vanadium cross-over from other causes of performance losses. Indeed, the duration of each cycles is fixed and thus the change in the SoC of the battery is independent from electrodes performance, ohmic losses and mass transport issues, but it depends only on the self-discharge due to vanadium cross-over fluxes, assuming negligible hydrogen evolution reactions. To mitigate possible influence of hydrogen evolution reactions, the current density was limited to 50 mA cm^{-2} and the SoC range in which the battery operated was chosen to avoid reaching high SoC at the negative electrode. In order to monitor the evolution of the battery SoC, the OCV of the battery is measured for 90 s after each charge and discharge. Since the duration of the charge and discharge semi-cycles are fixed and equal to have equal charged and discharged capacity, the coulombic efficiency in this type of cycles is always equal to 1 [50,51,66,67].

Before starting the charge-discharge cycles an EIS was performed imposing a 0 A steady current and a perturbation with 5 mA cm^{-2} amplitude at 50 frequencies logarithmically spaced in the range 100 kHz–1 Hz.

2.4. Electrochemical characterization for the ink flow rate analysis

2.4.1. Experimental set-up

The experimental set-up for the electrochemical characterization of the barrier layers deposited for the analysis of the ink flow rate consisted in a VRFB of 25 cm^2 active area with graphite interdigitated flow fields at both sides of the cell. Carbon felts (Sigracell® SGL 2.5 EA, nominal thickness 2.5 mm, compressed to 2 mm with glass-PTFE gaskets) were used as positive and negative electrodes. Positive and negative electrolyte solutions were prepared by charging at 50 mA cm^{-2} a commercial 1.6 M vanadium electrolyte solution in 2 M sulphuric acid (50% VO^{2+}/ 50% V^{3+}, *AMG Titanium Alloys & Coatings - GfE GmbH*). The same peristaltic pump and two SMU modules described in subsection 2.3.1 were used during the testing of the battery with the manufacturer barrier layer and the reference *Nafion*^{TM} NR212 membrane.

As stated in the introduction, one of the scope of the work is to test the scaled-up barrier in operative conditions more representative of the real applications. For this reason, the electrodes were changed from carbon papers to carbon felts, which are the state-of-the-art of the technology. Moreover, SGL2.5 EA are already thermally activated as received allowing to increase the current density during the testing. For the same reason the electrolyte solutions were changed to commercial electrolyte solution from lab-made solution.

A PerkinElmer Optima 8300 spectroscope was used to perform Inductively Coupled Plasma-Optical Emission Spectroscopy (ICP-OES) [68] on the vanadium electrolyte solutions to measure the vanadium concentration at the end of the tests for the estimation of the net vanadium transfer through the membrane.

2.4.2. Experimental tests

Each barrier layer and the reference *Nafion*^{TM} membrane were tested in charge-discharge cycles with cut-off voltages of 1.65 V and 1 V. A sequence of three current densities (50 mA cm^{-2}, 100 mA cm^{-2} and 150 mA cm^{-2}) steps for 3 cycles each was applied firstly to evaluate the performance of the battery with the different separators at different

current densities, then 150 cycles at 100 mA cm^{-2} were performed to evaluate the capacity decay of the battery and the performance stability. Finally, the initial sequence of current densities was repeated. The volumetric flow rate of the electrolyte solutions was 40 ml min^{-1} for each test, while the starting SoC was around 10 %. Before starting the charge-discharge cycles an EIS was performed imposing a 0 A steady current and a perturbation with 5 mA cm^{-2} amplitude at 50 frequencies logarithmically spaced in the range 100 kHz–1 Hz.

At the end of the cycles a sample from both electrolytes was taken to measure the vanadium concentration through ICP-OES analysis. From the concentration measurement was possible to estimate the net vanadium transfer through the membrane with a molar balance between the beginning and the end of the test [51]:

$$N_{net,vanadium} = \frac{\Delta n}{\Delta tA} \tag{2.3}$$

with Δn moles variation, Δt duration of the test and A area of the cell. The moles variation was computed from the initial and final concentrations and volumes of the electrolyte solutions.

2.5. Electrochemical characterization for scaled-up barrier layer

2.5.1. Experimental set-up

The characterization of the barrier layers of 100 cm^2 active area and a reference membrane *Nafion*^{TM} NR212 was conducted in a VRFB employing a flow-through cell architecture coupled with SGL 2.5 EA carbon felts. The cell architecture was changed with respect to the previous cases to test the barrier layer in the most common cell configuration for real VRFB applications [69]. As done in the previous section, the electrolyte solutions were prepared by charging at 50 mA cm^{-2} the commercial 1.6 M vanadium electrolyte solution in 2 M sulphuric acid (50% VO^{2+}/ 50% V^{3+}, *AMG Titanium Alloys & Coatings - GfE GmbH*).

A combination of a *National Instrument RMX 4124* power supply and a *Chroma DC 63610-80-20* electronic load was used to perform charge-discharge cycles on the scaled-up VRFB.

2.5.2. Experimental tests

The scaled-up barriers and the reference *Nafion*^{TM} NR212 membranes were tested in charge-discharge cycles with cut-off voltages of 1.65 V and 1 V. Like the tests described in Section 2.4.2, at the beginning of the cycles an initial sequence of three current densities (50, 100 and 150 mA cm^{-2}) was performed, followed by a series of cycles at 100 mA cm^{-2}. The cycling test lasted up until the discharge capacity of the battery fell below a lower limit, defined as the 80 % of the value of the capacity at the first cycle at 100 mA cm^{-2} of the reference *Nafion*^{TM} NR212. This threshold was chosen according to the work of Rodby et al. [11], where it was defined through a economical analysis the optimal limit for the battery capacity after which the electrolyte rebalancing procedures shall be performed.

3. Results and discussion

3.1. Influence of ink composition

3.1.1. Ionomer content analysis

Fig. 2A, B and 2C report SEM images of the cross-section of the barrier layers with different ionomer amount. In all three cases the silica and Vulcan® XC-72R nanoparticles organize in clusters of nanoparticles, introducing a tortuous path for the ion transport, instead the *Nafion*^{TM} ionomer covers the nanoparticles, as also shown by Energy Dispersive Spectroscopy (EDS) analysis, reported in the Supplementary Materials. Increasing the amount of ionomer with respect to the nanoparticles (I-NP ratio) lead to a more compact morphology of the barrier layer as the ionomer fills the void spaces between the clusters of nanoparticles.
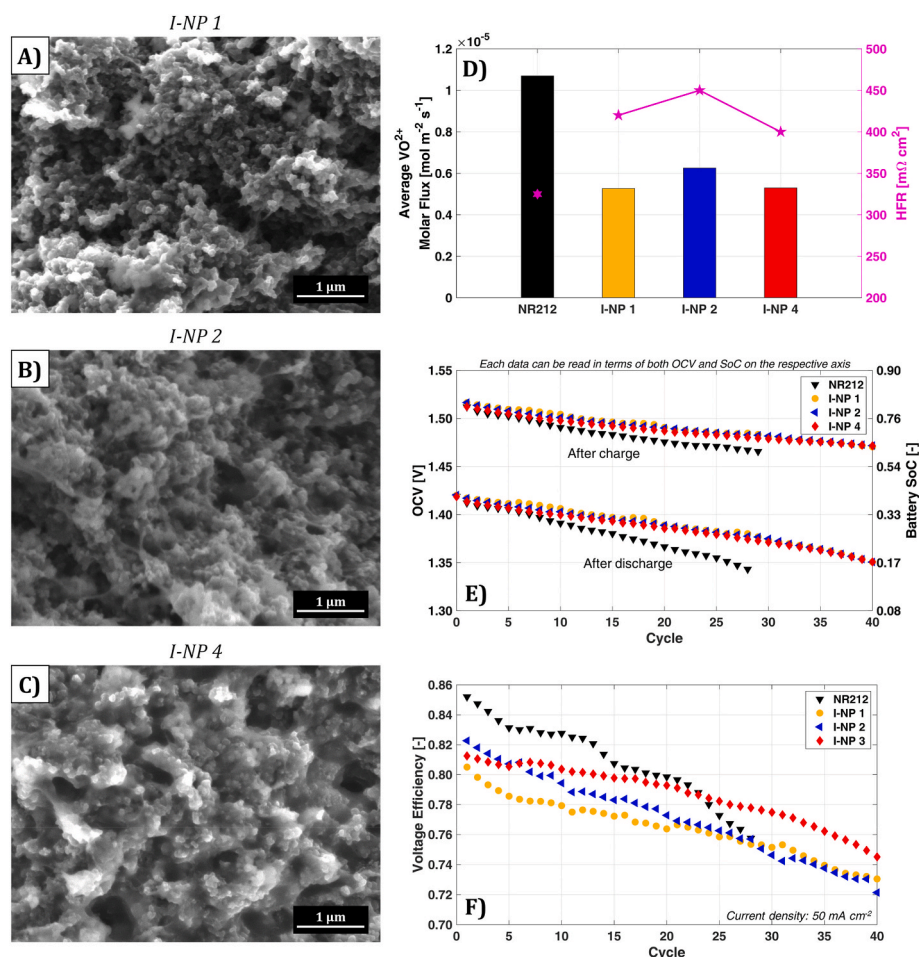
Fig. 2. SEM images of barrier layers cross-section on silicon wafers at different I-NP: A) 1, B) 2 and C) 4. D) Average vanadium fluxes during diffusion test (left axis) and HFR (magenta markers, right axis) with barriers on Nafion™ NR212 at different I-NP and for the reference Nafion™ NR212. E) Battery OCV (left axis) and SoC (right axis) and F) Voltage Efficiency during charge-discharge cycles at fixed capacity with barriers at different I-NP and the reference Nafion™ NR212. (For interpretation of the references to colour in this figure legend, the reader is referred to the Web version of this article.)

Indeed, with a I-NP of 1 (Fig. 2A) large pores can be observed, while with I-NP ratios of 2 and 4 (Fig. 2B and C) the barrier layers appear more compact. Fig. 5 of the Supplementary Materials reports the cross-sectional SEM images of the considered barrier layers: it highlights the uniform thickness of the layers and the fact that all thickness were coherent with the one by design.

As regards the influence of the I-NP on the ability of the barrier to mitigate cross-over, Fig. 2D compares the results of the diffusion tests of the barriers with different I-NP ratio and the reference membrane NR212: the introduction of the barrier allowed to significantly reduce the vanadium flux through the separator. In particular, the average flux was halved with respect the reference membrane in the case of the barriers with I-NP 1 and I-NP 4, reducing the average flux from $1.07 \times 10^{-5}\ mol\ m^{-2}\ s^{-1}$ with the bare membrane to $0.53 \times 10^{-5}\ mol\ m^{-2}\ s^{-1}$ for both barriers. Instead, for the I-NP 2 barrier it was reduced only by 42 % ($0.63 \times 10^{-5}\ mol\ m^{-2}\ s^{-1}$). Moreover, it is possible to estimate also the diffusivity of the VO^{2+} ions through the tested separators from the results of the diffusion tests. The resulting diffusivity was $5.34x10^{-13}\ m^2\ s^{-1}$ for the bare *Nafion™* NR212 membrane, while for the barrier layers the diffusivities resulted $3.17x10^{-13}\ m^2\ s^{-1}$, $3.76x10^{-13}\ m^2\ s^{-1}$ and $3.18x10^{-13} m^2\ s^{-1}$ for I-NP 1, I-NP 2 and I-NP 4 respectively. Regardless of the I-NP, the barrier layers significantly reduced the diffusivity of the VO^{2+} ions. Details of the calculation have been reported in the supplementary materials. Fig. 2D also reports the value of the HFR of the battery measured with EIS for the different

separators: the introduction of the additional selective layer led to an increase in the range 75–100 mΩ cm² in the HFR of the battery with respect to the bare membrane (325 mΩ cm²). In particular, the barrier with I-NP 4 showed the lower HFR (400 mΩ cm²), while the one with I-NP 2 showed the highest value (450 mΩ cm²). From the HFR of the battery and the overall thickness of the separator it is possible to calculate the overall conductivity of the sample: for the reference membrane it was equal to $1.54\ S\ m^{-1}$, while for the barrier layers ranged between $1.33\ S\ m^{-1}$ and $1.50\ S\ m^{-1}$. The barrier reduced the conductivity of the separators, but only by 2%–13 % than the bare membrane case. This trend of the HFR of the battery with respect to the ionomer content in the barrier layer can be associated to a trade-off between an improved network of ionomer, favoured by higher ionomer content, and higher barrier porosity, favoured by lower ionomer content, which allows the vanadium electrolyte to penetrate more in depth, thus shortening the ionic path through the barrier. The increase in the HFR of the battery with the barrier layers introduces larger ohmic losses with respect to the bare membrane and it may hinder the selectivity of the barrier layer if the reduction of the overall conductivity is higher than the reduction of the vanadium ions diffusivity. However, in all the cases presented in Fig. 2 the HFR increased by 23%–30 %, while the vanadium flux through the membrane during the diffusion test reduced by 42%–50 %, suggesting an analogous reduction of the VO^{2+} diffusivity. Therefore, it is possible to roughly estimate an increase in the selectivity of the membrane due to the barrier [51] between 20 % and 62 %, with the highest improvement occurred with the barrier with I-NP 4. It is also
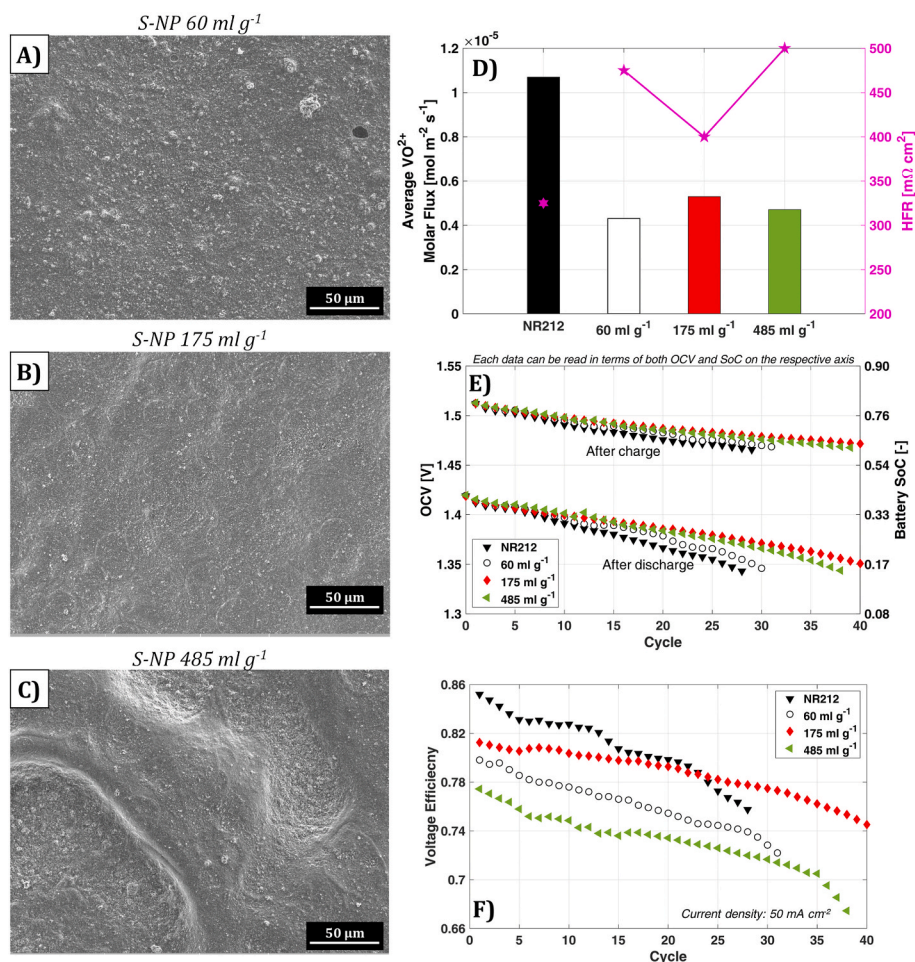
Fig. 3. SEM images of barrier layers top-view on silicon wafers at different S-NP: A) 60 ml g^{-1}, B) 175 ml g^{-1} and C) 485 ml g^{-1}. D) Average vanadium fluxes during diffusion test (left axis) and HFR (magenta markers, right axis) with barriers on Nafion™ NR212 at different S-NP and for the reference Nafion™ NR212. E) Battery OCV (left axis) and SoC (right axis) and F) Voltage Efficiency during charge-discharge cycles at fixed capacity with barriers at different S-NP and the reference Nafion™ NR212. (For interpretation of the references to colour in this figure legend, the reader is referred to the Web version of this article.)
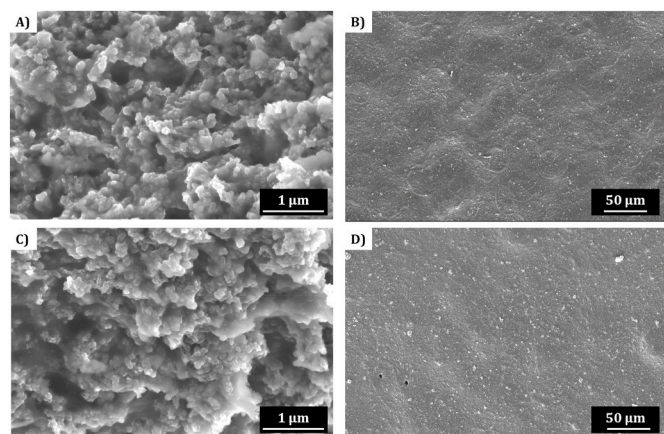

Fig. 4. – SEM images of barrier layers deposited on silicon wafers with different ink flow rate: A, B) 0.2 ml min^{-1}, cross-section view and top view respectively, and C, D) 0.5 ml min^{-1}, cross-section view and top view respectively.

possible to estimate the selectivity of the different separators as the ratio of the conductivity and vanadium diffusivity calculated previously. Because of the barrier, which hindered more the vanadium diffusivity than the proton conductivity, the selectivity was increased from $2.88x10^{12}$ S m^3 s with the bare membrane to $4.71x10^{12}$ S m^3 s (+64 %)

with the best case, the I-NP4, highlighting the selective ability of the barrier layer.

After demonstrating that the barrier layers manufactured through USC improve the selectivity of the membrane towards VO^{2+}, the influence of the barrier layers on battery performance was evaluated in charge-discharge cycle to assess the ability of the barrier layer during battery operation, in presence of more vanadium species and involved physical phenomena.

As regards the effect of the ion composition on the performance of the battery, Fig. 2E shows the evolution of the OCV and the SoC of the battery during charge-discharge cycles with fixed exchanged capacity due to the self-discharge caused by vanadium cross-over. It can also be observed that the loss of SoC per cycle was around 0.40 % $cycle^{-1}$ for all the tested barriers, while it was 0.63 % $cycle^{-1}$ for the bare membrane, confirming the ability of the barrier layers to mitigate cross-over fluxes through the separator. It is worth noting that, despite a higher VO^{2+} flux during the diffusion test (Fig. 2D), the barrier with I-NP 2 showed a similar self-discharge to the other barriers. This is due to fact that during the operation of the battery in charge-discharge cycles vanadium cross-over is a complex interplay of mechanisms and it involves all vanadium species [67,70], while in the diffusion test only one vanadium species is present and no current is applied to the cell. Fig. 2F reports the voltage
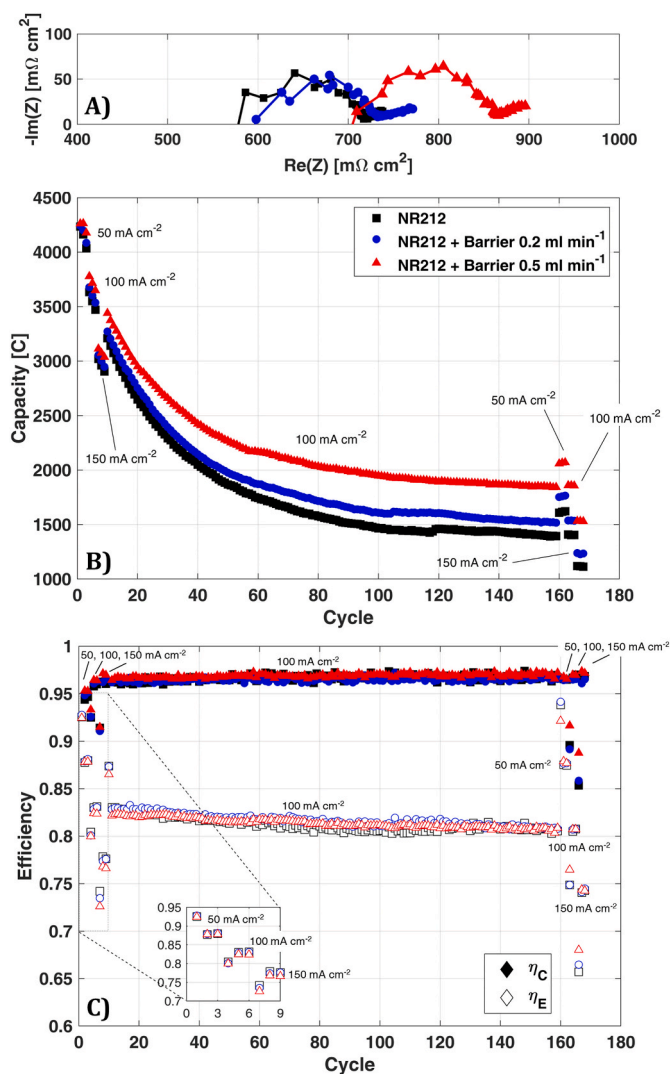
Fig. 5. – Electrochemical characterization of barrier layers on Nafion™ NR212 manufactured with different ink flow rate compared with reference Nafion™ NR212 membrane: A) Nyquist plot EIS spectra, B) discharged capacity during charge-discharge cycles with initial and final current density steps and C) coulombic and energy efficiencies during charge-discharge cycles. Miniature: energy efficiency at different current density during the first current steps.

efficiency during the cycles[2]: the starting efficiency is lower than the reference membrane for all barriers because of the higher HFR. However, due to the lower self-discharge due to cross-over, the batteries employing the barrier layers suffered a lower efficiency loss because of less unbalanced operation. Considering the average value of the efficiency on the first 28 cycles, i.e. the duration of the test with the *Nafion^{TM}* NR212 reference membrane, the barrier with I-NP 4 operated with an average value of 79.7 %, the highest among the tested barriers, which is around 1 % lower than the average for the reference case (80.9 %), while the barrier I-NP 1 and I-NP 2 operated with efficiency 77.2 % and 78.6 % respectively.

The analysis on the influence of the amount on ionomer in the barrier showed that the barrier layers can successfully mitigate the self-discharge of the battery due to cross-over by a third and that the I-NP has a negligible influence on the self-discharge of the battery. Among the

tested barriers, a I-NP ratio of 4 ensured the lowest HFR and the highest average efficiency. Given these reasons, the I-NP ratio of 4 was set as reference value of the ionomer content in the barrier layer for the rest of work for all barriers deposited after this analysis.

3.1.2. Ink dilution analysis

Fig. 3A, B and 3C report the SEM images of the top view of barrier layers deposited with inks with different dilution, i.e. different S-NP ratio. In this analysis the top views of the samples were considered, differently from the cross-sections of Fig. 2, as they allow to better understand the impact of the dilution level on the quality of the coating. Cross-sections of these barrier samples are reported in the Supplementary Materials (Figure S6 and Figure S7). The barrier layer deposited with S-NP 175 ml g^{-1} (Fig. 3B) presented a quite regular surface and an homogeneous coating, while decreasing or increasing the amount of solvent in the ink (Fig. 3A and C respectively) led to irregularity and heterogeneity in the coating. With a S-NP of 60 ml g^{-1} the top view (Fig. 3A) reports a high number of agglomerates of nanoparticles and ionomer on the surface of the barrier. These agglomerates were caused by two possible causes: it may consequence of either a not optimal dispersion of the dry fraction during the ink preparation due to the lower amount of dispersing medium or a too fast drying of all the solvent at the substrate, preventing the formation of a homogenous liquid film, or a combination of both causes. Instead, Fig. 3C shows the coating in the case of a very diluted ink (S-NP 485 ml g^{-1}): the surface of the barrier layer presented clear features of a not-optimal distribution of the ink on the substrate. Indeed, the larger quantity of solvent in the ink led to a very wet deposition that required more time for the complete drying of the deposited layer. This gave the ink droplets time to coalesce into larger droplets, forming small puddles that dried unevenly, as it can be seen in Fig. 3C.

Despite the reduced quality of the superficial coating with S-NP 60 ml g^{-1} and 485 ml g^{-1}, the barrier layer manufactured with these inks were still able to mitigate cross-over fluxes of vanadium through membrane during diffusion test, as it can be seen in Fig. 3D. Moreover, these barrier layers allowed a higher reduction of the vanadium flux with respect to the barrier with S-NP 175 ml g^{-1}. However, the barriers manufactured with both the more concentrated ink and the more diluted one increased the HFR of the battery by 75–100 mΩ cm^2 with respect to the barrier deposited with S-NP 175 ml g^{-1}. This increase in the HFR may be related to a less effective ionomer network in the barrier layer in terms of proton transfer due to the heterogeneous drying of the barrier layer caused by both a reduced amount and excessive quantity of solvent in the ink.

As regards the self-discharge of the battery during charge-discharge cycles, Fig. 3E shows that, despite a higher vanadium flux during the diffusion test, the barrier layer with S-NP 175 ml g^{-1} provided the lowest self-discharge for the battery. Indeed, the Soc loss per cycle was around 0.39 % cycle^{-1}, while it was 0.46 % cycle^{-1} in the case of the barrier made with the 485 ml g^{-1} S-NP ink and 0.56 % cycle^{-1} for the 60 ml g^{-1} one. It is worth mentioning that the diffusion test and the cycling testing showed discordant results due to the reasons explained above for the analysis of the ionomer content influence. Therefore, these results highlighted that the diffusion test is an useful technique for a first evaluation of the ability of a separator in mitigating cross-over fluxes, but it is not an effective solution for tuning the design parameters of the considered separator.

Fig. 3F reports the voltage efficiency during the cycling operation: the trend reflects the one of the HFR of Fig. 3D with the barrier made with the ink with S-NP 175 ml g^{-1} operating with the highest efficiency accordingly with the lowest HFR among the barriers, while the battery employing the barrier made with the 485 ml g^{-1} S-NP ink showed the lowest efficiency, consequence of the highest HFR.

Similarly to the analysis of the ink composition, it is possible to estimate the diffusivity of VO^{2+} ions and the conductivity from the results of the diffusion tests and HFR. The diffusivity of the barrier layers with

---

[2] In this type of cycles, the coulombic efficiency is in all cases equal to 1, therefore it is not reported. Consequently, the value of energy efficiency coincides with the voltage efficiency.

S-NP 60 $ml\,g^{-1}$ and 485 $ml\,g^{-1}$ were 2.59x10^{-13} $m^2\,s^{-1}$ and 2.83x10^{-13} $m^2\,s^{-1}$ respectively, significantly lower than the reference membrane and the barrier layer with S-NP 175 $ml\,g^{-1}$. As regards the conductivity, the diluted case and dilute case showed the lowest values of 1.26 $S\,m^{-1}$ and 1.20 $S\,m^{-1}$ respectively. Considering these values, the selectivity for the 60 $ml\,g^{-1}$ barrier layer was 4.88x10^{12} $S\,m^{-3}\,s$, while for the 485 $ml\,g^{-1}$ one it was 4.24x10^{12} $S\,m^{-3}\,s$.

The results reported in Fig. 3 showed that a S-NP ratio of 175 ml g^{-1} allowed to obtain both the lowest self-discharge during charge-discharge cycles at fixed exchanged capacity and the highest battery efficiency. Therefore, this value of S-NP ratio was set as reference value of the dilution level of the barrier ink for the rest of work after this analysis.

After the reference ink composition was identified with the results reported in Figs. 2 and 3 the focus of the investigation was shifted on the deposition process of the barrier layer to identify the influence of the process parameters on the barrier properties.

3.2. Deposition process parameters analysis

Fig. 4 compares the SEM images of two barrier layers deposited with different ink flow rate. Fig. 4A and B report the cross-section view and top view respectively of the barrier deposited with ink flow rate 0.2 ml min^{-1}. This barrier sample was manufactured with the same deposition process parameters and ink formulation of the barrier sample reported in Figs. 2C and 3B. It is possible to observe that the barrier layers show no difference in the morphology in both the cross-section and the top view, suggesting that the ink preparation and the spray coating are repeatable processes.

Instead, Fig. 4C and D reports the SEM images of the barrier layer deposited with ink flow rate 0.5 ml min^{-1}: the morphology of the barrier layer in the cross-section (Fig. 4C) showed little to no difference with respect to the deposited at 0.2 ml min^{-1}, as in both cases the nanoparticles of Vulcan® XC-72R and silica are covered by ionomer and organized in packed clusters with inter-clusters pores of diameter lower than 1 μm. As regards the top view, Fig. 4B and D presents some differences: at lower ink flow rate (Fig. 4B) a large quantity of coffee ring features can be identified, while at higher flow rate (Fig. 4D) they are absent, suggesting that the deposition at higher flow rate guaranteed a more uniform evaporation of the solvent [71]. However, Fig. 4D shows more superficial agglomerates of nanoparticles than Fig. 4B: since the two barrier layers were deposited with the same ink, the presence of more agglomerates is not caused by an improper ink formulation and preparation but it is due to the different deposition process. In particular, it can be associated to a nozzle atomization power lower than the optimal one for an ink flow rate of 0.5 ml min^{-1}.

Indeed, as indicated by the USC machine operating manual, the optimal nozzle power lies in a range between 0.5 W–1 W higher than the stall point, which is minimum nozzle to power to atomize the ink droplets without nozzle tip flooding [72]. The stall point depends both on the ink properties and high flow rate: increasing the flow rate from 0.2 ml min^{-1} to 0.5 ml min^{-1}, increased the stall point from 1.4 W to 1.7 W. As consequence, the nozzle power was simply increased by 0.3 W with respect to the barrier manufactured at 0.2 ml min^{-1} without an accurate tuning of this parameter, which would have required several more tests, since the quality of the coating showed no critical inhomogeneity.

Fig. S8 of the Supplementary Materials reports the cross-sectional SEM images of the barrier layers to compare them in terms of thickness uniformity, showing that in both cases the thickness was coherent with the designed one and uniform along the layer.

Fig. 4 showed that the morphology of the barrier layer remained the same also when the layer is manufactured with a higher ink flow rate. As regards the performance in a VRFB Fig. 5 reports the results of the electrochemical characterization: despite the similar morphological

structure, changing the ink flow rate led to differences in the barrier performance. Indeed, the barrier manufactured with ink flow rate 0.5 ml min^{-1} showed a 100 mΩ cm^2 increase in the HFR with respect to the case of 0.2 ml min^{-1} (Fig. 5A).[3] Since there is no difference in the morphology of the two barriers, the cause of this HFR difference is likely due to the interaction between the ink and the supporting membrane. Indeed, the solvent of the ink is ethanol which can cause the swelling of the membrane, enlarging the ionic clusters favouring the ion transport through the membrane [73]. In the case of these two barrier layers the overall amount of ink and solvent sprayed on the membrane is the same, but due to the differences in the ink flow rate, nozzle velocity and deposition pattern the solvent was distributed over the membrane surface differently in the two cases. The broader deposition pattern of the barrier layer deposited at 0.5 ml min^{-1} allowed to significantly reduce the amount of solvent deposited on the surface of the membrane per serpentine, facilitating its evaporation and thus preventing the possibility of micro-swelling of the membrane [73].

Fig. 5B reports the capacity decay of the battery during charge-discharge cycles with the reference *Nafion*^{TM} NR212 membrane and the studied barrier layers. The barrier layer manufactured at 0.2 ml min^{-1} showed a similar capacity decay than the bare membrane, thus showing limited advantages in terms of capacity decay mitigation. Instead, increasing the ink flow rate to 0.5 ml min^{-1} reduced the capacity decay of the battery allowing to discharge more capacity at all current density steps and during the 150 cycles at 100 mA cm^{-2} despite the higher HFR. In particular, considering the first and last cycles at 100 mA cm^{-2}, the bare *Nafion*^{TM} NR212 and the barrier manufactured at 0.2 ml min^{-1} had a capacity loss of 57 % and 54 % respectively, while the barrier at 0.5 ml min^{-1} the capacity loss was reduced to 46 %, showing the ability of the barrier layer to mitigate cross-over losses and capacity decay of the battery also in operating conditions more representative of the real applications. Moreover, the barrier at 0.5 ml min^{-1} reduced also the net vanadium transfer through the separator as reported in Table 2, where the net vanadium transfer was calculated from the vanadium concentration of the electrolytes at the end of test measured by ICP-EOS analysis by exploiting Equation (2.3). The barrier at 0.5 ml min^{-1} reduced the vanadium transfer through the membrane from 2.44 × 10^{-5} $mol\,m^{-2}\,s^{-1}$ with the bare membrane to 1.68 × 10^{-5} $mol\,m^{-2}\,s^{-1}$, which is a reduction of 31 %. Instead, the barrier at 0.2 ml min^{-1} reduced the net vanadium transfer only by 9 % with respect to the bare membrane, showing that increasing the ink flow rate during the deposition process allowed for a larger mitigation of both capacity decay and net vanadium transfer. As the case of the HFR, the improvement of the performance of the barrier due to the higher ink flow rate can be associated to the interaction between the solvent of the ink and the supporting membrane during the deposition of the barrier layer. Indeed, the

Table 2
ICP-OES analysis results of the vanadium concentration in the electrolytes at the end of the test and resulting average net vanadium flux through the separator.

	NR212	NR212 + Barrier 0.2 ml min^{-1}	NR212 + Barrier 0.5 ml min^{-1}
$C_{V,EOT}^{Pos}\,[g\,l^{-1}]$	106.90 ± 2.00	103.80 ± 2.00	98.70 ± 2.00
$C_{V,EOT}^{Neg}\,[g\,l^{-1}]$	55.82 ± 1.00	56.61 ± 1.00	62.63 ± 1.00
$N_V^{net}\,[mol\,m^{-2}s^{-1}]$	(2.44 ±0.12) × 10^{-5}	(2.21 ±0.15) × 10^{-5}	(1.68 ±0.11) × 10^{-5}

---

[3] It is worth noting that also that changing the electrodes type from thin carbon papers to thick carbon felts and modifying the electrolyte composition led to a change of the HFR of the battery also in the case of the reference membrane.

reduction of membrane micro-swelling reduced the proton conductivity and the vanadium diffusivity of the supporting membrane with different intensity, affecting more the vanadium diffusivity [74], improving thus the overall selectivity of the separator.

The results of the capacity decay reported in Fig. 5B for the barrier manufactured at 0.2 ml min^{-1} are apparently in disagreement with the results of the same type of barrier layer reported in Section 3.1. In the previous section the barrier at 0.2 ml min^{-1} prove to effectively reduce the self-discharge of the battery with respect to the bare membrane, while in Fig. 5B showed very minor improvement in the capacity decay mitigation. This is consequence of the change of the type of cycles performed and of the operating conditions. In particular, due to the lower operating current density and the high sulphuric acid molarity of the electrolytes of the charge-discharge cycles performed in Section 3.1 made diffusion the main driving force for cross-over fluxes [67,70]. Therefore, the overall additional mass transport resistance provided by the barrier allowed to reduce the self-discharge in the tests reported in Figs. 2E and 3E. Instead, higher operating current density and the lower acid molarity of the tests of Fig. 5B enhanced the contribution of the migrative fluxes independently by the thickness of the separator, as reported in Toja et al. [70]. These results highlight the importance of the operating conditions with which the testing is carried out: therefore, manufacturing and testing the barrier layer with commercial components valorise the obtained results, enhancing their relevance for the improvement of the technology.

As regards the impact of the barrier layer on the battery efficiency, Fig. 5C shows that both barrier layer led to not significant improvements in the coulombic efficiency, apart from the initial current steps where the 0.5 ml min^{-1} barrier operated with a coulombic efficiency 0.5 % higher than the bare membrane. The higher HFR of the barrier slightly penalized its voltage efficiency[4] with respect to the supporting membrane, resulting in a reduction in the range 0.5 %–1 % of the energy efficiency during the initial current steps. However, in the following 150 cycles at 100 mA cm^{-2} the average energy efficiency for the bare *Nafion*^{TM} NR212 was 81.2 %, while for the barrier was 81.7 % and 81.4 % for the 0.2 ml min^{-1} and 0.5 ml min^{-1} barriers respectively, showing that the reduction of cross-over fluxes due to the introduction of the barrier allowed to mitigate the performance losses due to battery self-discharge and unbalanced operations.

Fig. S9 of the Supplementary Materials compares photos of the surface of pristine and tested barrier layers, showing that the barrier layer was not removed or dissolved by the flowing electrolyte during the operation of the battery, highlighting the structural stability of the barrier layer, that, together to the stable efficiencies reported in Fig. 5, suggest that the barrier layer deposited with the USC is stable.

The morphological analysis of Fig. 4 and the electrochemical characterization reported in Fig. 5 proved not only that it possible to deposit the barrier layer with an higher ink flow rate, reducing the time required for a scaled-up manufacturing process, but it proved also that increasing the flow rate enables also improvements in the barrier performance. Therefore, the combination of ink flow rate 0.5 ml min^{-1} and nozzle velocity of 50 mm s^{-1} was chosen for the deposition process for the scale-up of the barrier layer, reported in the following Section.

3.3. Scale-up to 100 cm^2

Fig. 6A reports the discharged capacity during charge-discharge cycles for the batteries with active area 100 cm^2 and the flow through cell configuration. For each case, the test lasted until the discharged capacity reached a value lower than 11200 C, which is around 80 % of the capacity of the first cycle at 100 mA cm^{-2} for the bare *Nafion*^{TM} NR212 case. The barrier on *Nafion*^{TM} NR212 was able to successfully reduce the capacity decay with respect to the supporting membrane, allowing to
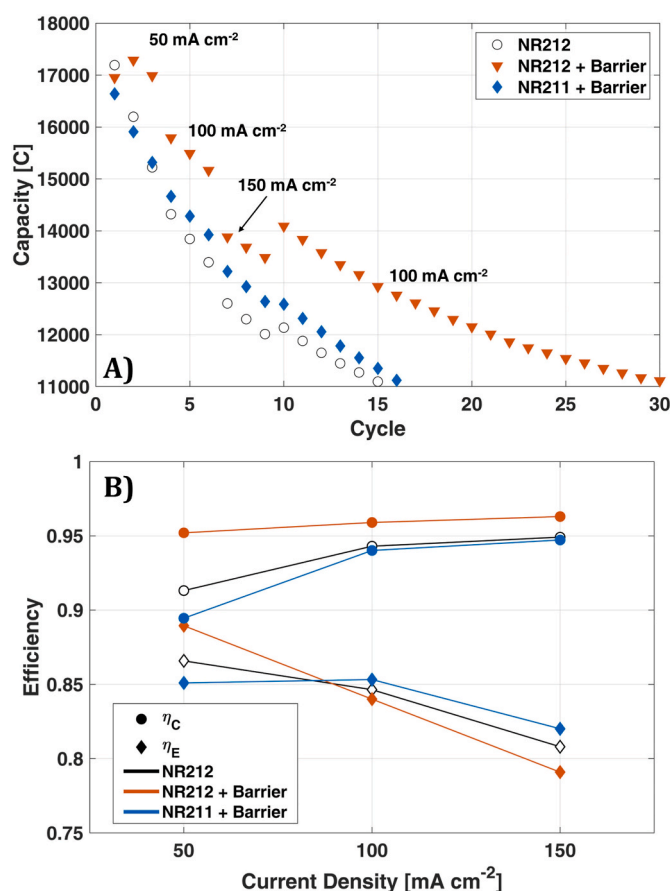

Fig. 6. – Charge-discharge cycles at 100 cm^2 with Nafion™ NR212 and the barrier layer deposited on Nafion™ NR212 and NR211: A) discharged capacity and B) coulombic (○) and energy average efficiencies (◇).

discharge more capacity during the initial current density steps and to reach the lower limit of capacity after 30 cycles, i.e. 15 cycles more that the bare *Nafion*^{TM} NR212, doubling them. This results proved that the developed barrier layer can mitigate the capacity loss due to cross-over not only at lab-scale, but also in a scale and operating conditions more representative of the real applications. Increasing the number of cycles required to reach the capacity limit allows to halve the number of remixing necessary during the operation of the battery, cutting the cost related to the maintenance of the battery, minimizing the stoppage time of the battery and increasing the overall storable energy in the battery.

Fig. 6A reports also the results with the barrier layer deposited on the thinner supporting membrane *Nafion*^{TM} NR211, the reduction of the substrate thickness increased the capacity decay with respect to the barrier on *Nafion*^{TM} NR212. However, the capacity decay was similar to the one of the bare *Nafion*^{TM} NR212 and the lower capacity limit was reached after 16 cycles, proving thus the ability of the developed barrier to enhance the selectivity of thin membranes. It is worth noting that, despite the same capacity decay with respect to the bare *Nafion*^{TM} NR212, the reduction of the thickness of the supporting membrane allowed to reduce the ohmic losses and to discharge a large capacity at 150 mA cm^{-2}.

As regards the efficiencies, Fig. 6B shows that the barrier on *Nafion*^{TM} NR212 allowed to increase the coulombic efficiency of the battery with respect to the bare membrane, with a 4 % increase at 50 mA cm^{-2} and a 2 % increase at 100 mA cm^{-2} and 150 mA cm^{-2}. The higher HFR reduced the voltage efficiency, slightly penalizing the energy efficiency at 100 mA cm^{-2} and 150 mA cm^{-2}. Instead, at 50 mA cm^{-2} the higher coulombic efficiency with the barrier allowed to have a 2.5 % increase in the energy efficiency with respect to the bare membrane. Considering

---

[4] Not reported in the figure to improve its readability.

the barrier on *Nafion^{TM}* NR211, the reduction of the membrane thickness nullified the improvement in the coulombic efficiency, but it still allowed to obtain a coulombic efficiency equal to the one of the bare *Nafion^{TM}* NR212 despite the lower thickness of the membrane at 100 mA cm^{-2} and 150 mA cm^{-2}, while at 50 mA cm^{-2} operated with a 1 % lower coulombic efficiency. Nevertheless, the reduction of the membrane thickness allowed to reduce ohmic losses and improve the voltage efficiency, resulting in higher energy efficiency at 100 mA cm^{-2} (+0.7 %) and 150 mA cm^{-2} (+1.2 %).

The results reported in Fig. 6 proved that the Ultrasonic Spray Coating is able to manufacture a barrier layer that can mitigate cross-over losses not only at lab-scale, but it can also be easily and effectively scaled up to larger scales, more representative of the real operation. The developed barrier layer on *Nafion^{TM}* NR212 halved the capacity decay with respect to the supporting membrane, while the same barrier deposited on *Nafion^{TM}* NR211 allowed to improve the energy efficiency at high current density, without sacrificing the capacity of the battery with respect to the bare *Nafion^{TM}* NR212.

The results of the scaled-up components showed that the selective ability of the barrier allows to improve battery performance both with the reference membrane and the thinner membrane according to the operating conditions. In particular, at low current density operations the barrier used in combination with a thicker membrane reduces the capacity decay and improves the coulombic efficiency, while for high current density operation the barrier coupled with a thinner membrane improves the energy efficiency without sacrificing battery capacity. Moreover, the flexibility of the USC process in terms of ink composition and supporting substrate would allow for a fine-tuning of the barrier layer proprieties according to the application.

4. Conclusions

In this work the possibility of manufacturing a selective layer for membrane for VRFB applications by Ultrasonic Spray Coating was investigated by analysing the influence of the ink composition and of the deposition process on the ability of the barrier to mitigate cross-over. Finally, the barrier was scaled-up to 100 cm^2 to assess the ability of the Ultrasonic Spray Coating technique to manufacture a selective layer able to mitigate cross-over losses also at scales more representative of the real applications.

The main conclusions of the work are the following ones.

- Increasing the ionomer content in the barrier layer allows to obtain a more compact structure, but the influence on the battery self-discharge is limited. However, a higher content of ionomer in the barrier layer allowed to obtain a higher battery efficiency.
- The dilution of the barrier ink influences the way in which the solid fraction of the barrier layer reorganizes during the drying process of the solvent. An intermediate dilution level allows to reduce swelling and flooding phenomena and to obtain a homogenous layer, reducing self-discharge without compromising the battery efficiency.
- Increasing the ink flow rate, while also proportionally increasing the nozzle velocity to avoid intense swelling phenomena, caused no modification of the morphology of the barrier layer, therefore reducing the time required for fabrication. Moreover, due to a lower exposition to the solvent of the ink, the deposition at higher flow rate enabled to mitigate micro-swelling phenomena of the membrane, improving the performance of the separator.
- The barrier layer was successfully deposited with an active area of 100 cm^2 and successfully tested in a VRFB, proving that the USC can be easily scaled-up for the fabrication of the barrier without affecting the performance of the barrier layer. Moreover, the barrier layer was deposited on *Nafion^{TM}* NR211 allowing to improve the energy efficiency of the battery and showing that USC be used for the fabrication of thin membranes.

This work proved the possibility of depositing a selective layer on *Nafion^{TM}* membranes. However, given the wide range of material the USC technique can be used with, the selective layer can be also deposited over different types of membrane beyond *Nafion^{TM}*. To do that a tuning of the ink composition and deposition process are necessary according to the adopted membrane, particularly considering the interaction between the ionomer of the layer and the one of the supporting membrane, as well as the tendency of the support to swell.

CRediT authorship contribution statement

Marco Cecchetti: Writing – original draft, Visualization, Validation, Methodology, Investigation, Formal analysis, Data curation, Conceptualization. **Simone Fiorini Granieri:** Methodology, Investigation. **Fabio Di Fonzo:** Resources. **Damiano Fustinoni:** Methodology, Investigation. **Alfonso Niro:** Resources. **Andrea Casalegno:** Supervision, Project administration. **Matteo Zago:** Writing – review & editing, Visualization, Supervision, Resources, Project administration, Methodology, Funding acquisition, Conceptualization.

Declaration of competing interest

The authors declare that they have no known competing financial interests or personal relationships that could have appeared to influence the work reported in this paper.

Appendix A. Supplementary data

Supplementary data to this article can be found online at https://doi.org/10.1016/j.jpowsour.2024.235908.

Data availability

The data that has been used is confidential.

References

[1] International Energy Agency, Renewables 2023. https://www.iea.org/reports/renewables-2023, 2024.

[2] J.A. Dowling, K.Z. Rinaldi, T.H. Ruggles, S.J. Davis, M. Yuan, F. Tong, N.S. Lewis, K. Caldeira, Role of long-duration energy storage in variable renewable electricity systems, Joule 4 (2020) 1907–1928, https://doi.org/10.1016/j.joule.2020.07.007.

[3] S. Giarola, A. Molar-Cruz, K. Vaillancourt, O. Bahn, L. Sarmiento, A. Hawkes, M. Brown, The role of energy storage in the uptake of renewable energy: a model comparison approach, Energy Pol. 151 (2021), https://doi.org/10.1016/j.enpol.2021.112159.

[4] N. Poli, C. Bonaldo, M. Moretto, M. Guarnieri, Techno-economic assessment of future vanadium flow batteries based on real device/market parameters, Appl. Energy 362 (2024), https://doi.org/10.1016/j.apenergy.2024.122954.

[5] E. Sánchez-Díez, E. Ventosa, M. Guarnieri, A. Trovò, C. Flox, R. Marcilla, F. Soavi, P. Mazur, E. Aranzabe, R. Ferret, Redox flow batteries: status and perspective towards sustainable stationary energy storage, J. Power Sources 481 (2021) 228804, https://doi.org/10.1016/j.jpowsour.2020.228804.

[6] E. Sánchez-Díez, E. Ventosa, M. Guarnieri, A. Trovò, C. Flox, R. Marcilla, F. Soavi, P. Mazur, E. Aranzabe, R. Ferret, Redox flow batteries: status and perspective towards sustainable stationary energy storage, J. Power Sources 481 (2021), https://doi.org/10.1016/j.jpowsour.2020.228804.

[7] A. Clemente, R. Costa-Castelló, Redox flow batteries: a literature review oriented to automatic control, Energies 13 (2020) 1–31, https://doi.org/10.3390/en13174514.

[8] L. Cao, M. Skyllas-Kazacos, C. Menictas, J. Noack, A review of electrolyte additives and impurities in vanadium redox flow batteries, J. Energy Chem. (2018), https://doi.org/10.1016/j.jechem.2018.04.007.

[9] A.Z. Weber, M.M. Mench, J.P. Meyers, P.N. Ross, J.T. Gostick, Q. Liu, Redox flow batteries: a review, J. Appl. Electrochem. 41 (2011) 1137–1164, https://doi.org/10.1007/s10800-011-0348-2.

[10] K.W. Knehr, E. Agar, C.R. Dennison, A.R. Kalidindi, E.C. Kumbur, A transient vanadium flow battery model incorporating vanadium crossover and water transport through the membrane, J. Electrochem. Soc. 159 (2012) A1446–A1459, https://doi.org/10.1149/2.017209jes.

[11] K.E. Rodby, T.J. Carney, Y. Ashraf Gandomi, J.L. Barton, R.M. Darling, F. R. Brushett, Assessing the levelized cost of vanadium redox flow batteries with capacity fade and rebalancing, J. Power Sources 460 (2020) 227958, https://doi.org/10.1016/j.jpowsour.2020.227958.

[12] J.H. Vinco, A.E.E. da C. Domingos, D.C.R. Espinosa, J.A.S. Tenório, M. dos, P. G. Baltazar, Unfolding the Vanadium Redox Flow Batteries: an ineep perspective on its components and current operation challenges, J. Energy Storage 43 (2021) 103180, https://doi.org/10.1016/j.est.2021.103180.

[13] Y. Lei, B.W. Zhang, B.F. Bai, T.S. Zhao, A transient electrochemical model incorporating the Donnan effect for all-vanadium redox flow batteries, J. Power Sources 229 (2015) 202–211, https://doi.org/10.1016/j.jpowsour.2015.08.100.

[14] A. Trovò, F. Picano, M. Guarnieri, Comparison of energy losses in a 9 kW vanadium redox flow battery, J. Power Sources 440 (2019) 227144, https://doi.org/10.1016/j.jpowsour.2019.227144.

[15] Y.S. Chen, S.Y. Ho, H.W. Chou, H.J. Wei, Modeling the effect of shunt current on the charge transfer efficiency of an all-vanadium redox flow battery, J. Power Sources 390 (2018) 168–175, https://doi.org/10.1016/j.jpowsour.2018.04.042.

[16] B. Jiang, L. Wu, L. Yu, X. Qiu, J. Xi, A comparative study of Nafion series membranes for vanadium redox flow batteries, J. Membr. Sci. 510 (2016) 18–26, https://doi.org/10.1016/j.memsci.2016.03.007.

[17] Y. Shi, C. Eze, B. Xiong, W. He, H. Zhang, T.M. Lim, A. Ukil, J. Zhao, Recent development of membrane for vanadium redox flow battery applications: a review, Appl. Energy 238 (2019) 202–224, https://doi.org/10.1016/j.apenergy.2018.12.087.

[18] M. Cecchetti, M. Messaggi, A. Casalegno, M. Zago, Design and development of flow fields with multiple inlets or outlets in vanadium redox flow batteries, Batteries 10 (2024), https://doi.org/10.3390/batteries10030108.

[19] M. Messaggi, C. Gambaro, A. Casalegno, M. Zago, Development of innovative flow fields in a vanadium redox flow battery: design of channel obstructions with the aid of 3D computational fluid dynamic model and experimental validation through locally-resolved polarization curves, J. Power Sources 526 (2022) 231155, https://doi.org/10.1016/j.jpowsour.2022.231155.

[20] M. Wu, M. Liu, G. Long, K. Wan, Z. Liang, T.S. Zhao, A novel high-energy-density positive electrolyte with multiple redox couples for redox flow batteries, Appl. Energy 136 (2014) 576–581, https://doi.org/10.1016/j.apenergy.2014.09.076.

[21] H.R. Jiang, J. Sun, L. Wei, M.C. Wu, W. Shyy, T.S. Zhao, A high power density and long cycle life vanadium redox flow battery, Energy Storage Mater. 24 (2020) 529–540, https://doi.org/10.1016/j.ensm.2019.07.005.

[22] R. Wang, Y. Li, Carbon electrodes improving electrochemical activity and enhancing mass and charge transports in aqueous flow battery: status and perspective, Energy Storage Mater. 31 (2020) 230–251, https://doi.org/10.1016/j.ensm.2020.06.012.

[23] S. Corcuera, M. Skyllas-Kazacos, State-of-Charge monitoring and electrolyte rebalancing methods for the vanadium redox flow battery, Eur. Chem. Bull. 1 (2012) 511–519, https://doi.org/10.1016/j.jpowsour.2011.06.080.

[24] V. Viswanathan, A. Crawford, D. Stephenson, S. Kim, W. Wang, B. Li, G. Coffey, E. Thomsen, G. Graff, P. Balducci, M. Kintner-Meyer, V. Sprenkle, Cost and performance model for redox flow batteries, J. Power Sources (2014), https://doi.org/10.1016/j.jpowsour.2012.12.023.

[25] C. Minke, U. Kunz, T. Turek, Techno-economic assessment of novel vanadium redox flow batteries with large-area cells, J. Power Sources 361 (2017) 105–114, https://doi.org/10.1016/j.jpowsour.2017.06.066.

[26] C. Minke, M.A. Dorantes Ledesma, Impact of cell design and maintenance strategy on life cycle costs of vanadium redox flow batteries, J. Energy Storage 21 (2019) 571–580, https://doi.org/10.1016/j.est.2018.12.019.

[27] D. Düerkop, H. Widdecke, C. Schilde, U. Kunz, A. Schmiemann, Polymer membranes for all-vanadium redox flow batteries: a review, Membranes 11 (2021) 1–54, https://doi.org/10.3390/membranes11030214.

[28] L. Zeng, T.S. Zhao, L. Wei, H.R. Jiang, M.C. Wu, Anion exchange membranes for aqueous acid-based redox flow batteries: current status and challenges, Appl. Energy 233–234 (2019) 622–643, https://doi.org/10.1016/j.apenergy.2018.10.063.

[29] L. Zeng, Y. Ren, L. Wei, X. Fan, T. Zhao, Asymmetric porous polybenzimidazole membranes with high conductivity and selectivity for vanadium redox flow batteries, Energy Technol. 8 (2020) 1–8, https://doi.org/10.1002/ente.202000592.

[30] Y.H. Wan, J. Sun, Q.P. Jian, X.Z. Fan, T.S. Zhao, A detachable sandwiched polybenzimidazole-based membrane for high-performance aqueous redox flow batteries, J. Power Sources 526 (2022) 231139, https://doi.org/10.1016/j.jpowsour.2022.231139.

[31] Y.H. Wan, J. Sun, H.R. Jiang, X.Z. Fan, T.S. Zhao, A highly-efficient composite polybenzimidazole membrane for vanadium redox flow battery, J. Power Sources 489 (2021) 229502, https://doi.org/10.1016/j.jpowsour.2021.229502.

[32] Q. Dai, Z. Liu, L. Huang, C. Wang, Y. Zhao, Q. Fu, H. Zhang, X. Li, Thin-film composite membrane breaking the trade-off between conductivity and selectivity for a flow battery, Nat. Commun. 11 (2020) 1–9, https://doi.org/10.1038/s41467-019-13704-2|.

[33] Q. Dai, W. Lu, Y. Zhao, H. Zhang, X. Zhu, X. Li, Advanced scalable zeolite "ions-sieving" composite membranes with high selectivity, J. Membr. Sci. 595 (2020) 117569, https://doi.org/10.1016/j.memsci.2019.117569.

[34] W. Lee, M. Jung, D. Serhiichuk, C. Noh, G. Gupta, C. Harms, Y. Kwon, D. Henkensmeier, Layered composite membranes based on porous PVDF coated with a thin, dense PBI layer for vanadium redox flow batteries, J. Membr. Sci. 591 (2019), https://doi.org/10.1016/j.memsci.2019.117333.

[35] C. Sun, E. Negro, A. Nale, G. Pagot, K. Vezzù, T.A. Zawodzinski, L. Meda, C. Gambaro, V. Di Noto, An efficient barrier toward vanadium crossover in redox flow batteries: the bilayer [Nafion/(WO3)x] hybrid inorganic-organic membrane, Electrochim. Acta 378 (2021), https://doi.org/10.1016/j.electacta.2021.138133.

[36] J. Ye, X. Zhao, Y. Ma, J. Su, C. Xiang, K. Zhao, M. Ding, C. Jia, L. Sun, Hybrid membranes dispersed with superhydrophilic TiO2 nanotubes toward ultra-stable and high-performance vanadium redox flow batteries, Adv. Energy Mater. 10 (2020) 1904041, https://doi.org/10.1002/aenm.201904041.

[37] L. Zeng, J. Ye, J. Zhang, J. Liu, C. Jia, A promising SPEEK/MCM composite membrane for highly efficient vanadium redox flow battery, Surf. Coat. Technol. 358 (2019) 167–172, https://doi.org/10.1016/j.surfcoat.2018.11.018.

[38] Y. Zhang, Y. Zhong, W. Bian, W. Liao, X. Zhou, F. Jiang, Robust proton exchange membrane for vanadium redox flow batteries reinforced by silica-encapsulated nanocellulose, J. Hydrog. Energy. 45 (2020) 9803–9810, https://doi.org/10.1016/j.ijhydene.2020.01.188.

[39] J. Ye, D. Yuan, M. Ding, Y. Long, T. Long, L. Sun, C. Jia, A cost-effective nafion/lignin composite membrane with low vanadium ion permeation for high performance vanadium redox flow battery, J. Power Sources 482 (2021) 229023, https://doi.org/10.1016/j.jpowsour.2020.229023.

[40] D. Zhang, Q. Wang, S. Peng, X. Yan, X. Wu, G. He, An interface-strengthened cross-linked graphene oxide/Nafion212 composite membrane for vanadium flow batteries, J. Membr. Sci. 587 (2019) 117189, https://doi.org/10.1016/j.memsci.2019.117189.

[41] X. Lou, J. Ye, L. Xia, S. Chang, X. Zhao, C. Wu, M. Ding, Highly efficient and low cost SPEEK/TiO2 nanocomposite membrane for vanadium redox flow battery, J. Nanosci. Nanotechnol. 19 (2018) 2247–2252, https://doi.org/10.1166/jnn.2019.16467.

[42] L. Qiao, H. Zhang, W. Lu, Q. Dai, X. Li, Advanced porous membranes with tunable morphology regulated by ionic strength of nonsolvent for flow battery, ACS Appl. Mater. Interfaces 11 (2019) 24107–24113, https://doi.org/10.1021/acsami.9b06142.

[43] X. Yang, H. Zhu, F. Jiang, X. Zhou, Notably enhanced proton conductivity by thermally-induced phase-separation transition of Nafion/Poly(vinylidene fluoride) blend membranes, J. Power Sources 473 (2020) 1–9, https://doi.org/10.1016/j.jpowsour.2020.228586.

[44] Y. Chen, S. Zhang, Q. Liu, X. Jian, Sulfonated component-incorporated quaternized poly(phthalazinone ether ketone) membranes with improved ion selectivity, stability and water transport resistance in a vanadium redox flow battery, RSC Adv. 9 (2019) 26097–26108, https://doi.org/10.1039/c9ra05111b.

[45] H. Zhang, Z. Li, L. Hu, L. Gao, M. Di, Y. Du, X. Yan, Y. Dai, S. Ruan, G. He, Covalent/ionic co-crosslinking constructing ultra-densely functionalized ehter-free poly(biphenylene piperidium) amphoteric membranes for vanadium redox flow batteries, Electrochim. Acta 359 (2020) 136879, https://doi.org/10.1016/j.electacta.2020.136879.

[46] X. Yan, H. Zhang, Z. Hu, L. Li, L. Hu, Z. Li, L. Gao, Y. Dai, X. Jian, G. He, Amphoteric-side-chain-Functionalized "ether-free" poly(arylene piperidinium) membrane for advanced redox flow battery, ACS Appl. Mater. Interfaces 11 (2019) 44315–44324, https://doi.org/10.1021/acsami.9b15872.

[47] H. Wei, Y. Liu, W. Xu, J. Liu, C. Yan, X. Che, J. Yang, J. Tong, W. Xiao, Communication—polyethylene/PBI pore-filling composite membrane for high performance vanadium redox flow battery, J. Electrochem. Soc. 166 (2019) A3207–A3209, https://doi.org/10.1149/2.0271914jes.

[48] S.W. Choi, T.H. Kim, S.W. Jo, J.Y. Lee, S.H. Cha, Y.T. Hong, Hydrocarbon membranes with high selectivity and enhanced stability for vanadium redox flow battery applications: comparative study with sulfonated poly(ether sulfone)s and sulfonated poly(thioether ether sulfone)s, Electrochim. Acta 259 (2018) 427–439, https://doi.org/10.1016/j.electacta.2018.10.121.

[49] J. Hu, D. Yu, T. Li, H. Zhang, Z. Yuan, X. Li, A highly stable membrane with hierarchical structure for wide pH range flow batteries, J. Energy Chem. 56 (2021) 80–86, https://doi.org/10.1016/j.jechem.2020.07.043.

[50] M. Cecchetti, T.A. Ebaugh, H. Yu, L. Bonville, C. Gambaro, L. Meda, R. Maric, A. Casalegno, M. Zago, Design and development of an innovative barrier layer to mitigate crossover in vanadium redox flow batteries, J. Electrochem. Soc. 167 (2020) 130525, https://doi.org/10.1149/1945-7111/abbbbb.

[51] M. Cecchetti, T.A. Ebaugh, L. Bonville, R. Maric, A. Casalegno, M. Zago, Development of a vanadium redox flow battery operating with thin membrane coupled with a highly selective and stable silica-based barrier layer, Energy Technol. 2400410 (2024) 1–12, https://doi.org/10.1002/ente.202400410.

[52] N. Zhang, B. Yang, J. Huo, W. Qi, X. Zhang, X. Ruan, J. Bao, G. He, Hydration structures of vanadium/oxovanadium cations in the presence of sulfuric acid: a

molecular dynamics simulation study, Chem. Eng. Sci. 195 (2019) 683–692, https://doi.org/10.1016/j.ces.2018.10.014.

[53] V. Yarlagadda, S.E. McKinney, C.L. Keary, L. Thompson, B. Zulevi, A. Kongkanand, Preparation of PEMFC electrodes from milligram-amounts of catalyst powder, J. Electrochem. Soc. 164 (2017) F845–F849, https://doi.org/10.1149/2.1461707jes.

[54] X. Peng, P. Satjaritanun, Z. Taie, L. Wiles, A. Keane, C. Capuano, I.V. Zenyuk, N. Danilovic, Insights into interfacial and bulk transport phenomena affecting proton exchange membrane water electrolyzer performance at ultra-low iridium loadings, Adv. Sci. 8 (2021) 1–9, https://doi.org/10.1002/advs.202102950.

[55] S.A. Mauger, J.R. Pfeilsticker, M. Wang, S. Medina, A.C. Yang-Neyerlin, K. C. Neyerlin, C. Stetson, S. Pylypenko, M. Ulsh, Fabrication of high-performance gas-diffusion-electrode based membrane-electrode assemblies, J. Power Sources 450 (2020) 227581, https://doi.org/10.1016/j.jpowsour.2019.227581.

[56] Z. Turtayeva, F. Xu, J. Dillet, K. Mozet, R. Peignier, A. Celzard, G. Maranzana, The influence of ink formulation and preparation on the performance of proton-exchange membrane fuel cell, Energies 16 (2023), https://doi.org/10.3390/en16227519.

[57] T. Thornber, O.S. Game, E.J. Cassella, M.E. O'Kane, J.E. Bishop, T.J. Routledge, T. I. Alanazi, M. Togay, P.J.M. Isherwood, L.C. Infante-Ortega, D.B. Hammond, J. M. Walls, D.G. Lidzey, Nonplanar spray-coated perovskite solar cells, ACS Appl. Mater. Interfaces 14 (2022) 37587–37594, https://doi.org/10.1021/acsami.2c05085.

[58] Sono-Tek, Equipment solutions. https://www.sono-tek.com/products/, 2022.

[59] P.C. Ghimire, A. Bhattarai, R. Schweiss, G.G. Scherer, N. Wai, Q. Yan, A comprehensive study of electrode compression effects in all vanadium redox flow batteries including locally resolved measurements, Appl. Energy 230 (2018) 974–982, https://doi.org/10.1016/j.apenergy.2018.09.049.

[60] D.S. Aaron, Q. Liu, Z. Tang, G.M. Grim, A.B. Papandrew, A. Turhan, T. A. Zawodzinski, M.M. Mench, Dramatic performance gains in vanadium redox flow batteries through modified cell architecture, J. Power Sources 206 (2012) 450–453, https://doi.org/10.1016/j.jpowsour.2011.12.026.

[61] Y.A. Gandomi, D.S. Aaron, J.R. Houser, M.C. Daugherty, J.T. Clement, A. M. Pezeshki, T.Y. Ertugrul, D.P. Moseley, M.M. Mench, Critical review—experimental diagnostics and material characterization techniques used on redox flow batteries, J. Electrochem. Soc. (2018), https://doi.org/10.1149/2.0601805jes.

[62] J.M. F, R.P. Brooker, C.J. Bell, L.J. Bonville, H.R. Kunz, Determining vanadium concentrations using the UV-vis response method determining vanadium concentrations using the UV-vis response method, J. Electrochem. Soc. 162 (2015) A608–A613, https://doi.org/10.1149/2.0371504jes.

[63] D.N. Buckley, X. Gao, R.P. Lynch, N. Quill, M.J. Leahy, Towards optical monitoring of vanadium redox flow batteries (VRFBs): an investigation of the underlying

[64] spectroscopy, J. Electrochem. Soc. 161 (2014) A524–A534, https://doi.org/10.1149/2.023404jes.

[64] N.H. Choi, S. Kwon, H. Kim, Analysis of the oxidation of the V(II) by dissolved oxygen using UV-visible spectrophotometry in a vanadium redox flow battery, J. Electrochem. Soc. 160 (2013) A973–A979, https://doi.org/10.1149/2.145306jes.

[65] K.H. Shin, C.S. Jin, J.Y. So, S.K. Park, D.H. Kim, S.H. Yeon, Real-time monitoring of the state of charge (SOC) in vanadium redox-flow batteries using UV–Vis spectroscopy in operando mode, J. Energy Storage 27 (2020) 101066, https://doi.org/10.1016/j.est.2019.101066.

[66] M. Cecchetti, A. Casalegno, M. Zago, Local potential measurement through reference electrodes in vanadium redox flow batteries: evaluation of overpotentials and electrolytes imbalance, J. Power Sources 400 (2018) 218–224, https://doi.org/10.1016/j.jpowsour.2018.08.033.

[67] M. Cecchetti, F. Toja, A. Casalegno, M. Zago, A comprehensive experimental and modelling approach for the evaluation of cross-over fluxes in vanadium redox flow battery, J. Energy Storage 68 (2023) 107846, https://doi.org/10.1016/j.est.2023.107846.

[68] A. Fiorati, F. Florit, A. Mazzei, S. Buzzaccaro, B. Rossi, R. Piazza, R. Rota, L. De Nardo, Dispersions of zirconia nanoparticles close to the phase boundary of surfactant-free ternary mixtures, Langmuir 37 (2021) 4072–4081, https://doi.org/10.1021/acs.langmuir.0c03401.

[69] K. Lourenssen, J. Williams, F. Ahmadpour, R. Clemmer, S. Tasnim, Vanadium redox flow batteries: a comprehensive review, J. Energy Storage 25 (2019) 100844, https://doi.org/10.1016/j.est.2019.100844.

[70] F. Toja, L. Perlini, D. Facchi, A. Casalegno, M. Zago, Dramatic mitigation of capacity decay and volume variation in vanadium redox flow batteries through modified preparation of electrolytes, Appl. Energy 354 (2024) 122262, https://doi.org/10.1016/j.apenergy.2023.122262.

[71] S. Bose, S.S. Keller, T.S. Alstrøm, A. Boisen, K. Almdal, Process optimization of ultrasonic spray coating of polymer films, Langmuir 29 (2013) 6911–6919, https://doi.org/10.1021/la4010246.

[72] Z. Turtayeva, F. Xu, J. Dillet, K. Mozet, R. Peignier, A. Celzard, G. Maranzana, Manufacturing catalyst-coated membranes by ultrasonic spray deposition for PEMFC: identification of key parameters and their impact on PEMFC performance, Int. J. Hydrogen Energy 47 (2022) 16165–16178, https://doi.org/10.1016/j.ijhydene.2022.03.043.

[73] S. Song, W. Zhou, J. Tian, R. Cai, G. Sun, Q. Xin, S. Kontou, P. Tsiakaras, Ethanol crossover phenomena and its influence on the performance of DEFC, J. Power Sources 145 (2005) 266–271, https://doi.org/10.1016/j.jpowsour.2004.12.065.

[74] B. Jiang, L. Yu, L. Wu, D. Mu, L. Liu, J. Xi, X. Qiu, Insights into the impact of the nafion membrane pretreatment process on vanadium flow battery performance, Appl. Mater. Interfaces 8 (2016) 12228–12238, https://doi.org/10.1021/acsami.6b03529.